Science Advances
AAAS

advances.sciencemag.org/cgi/content/full/6/19/eaay6193/DC1

Supplementary Materials for

Evolution of vegetation and climate variability on the Tibetan Plateau over the past 1.74 million years

Yan Zhao*, Polychronis C. Tzedakis, Quan Li, Feng Qin, Qiaoyu Cui, Chen Liang, H. John B. Birks, Yaoliang Liu, Zhiyong Zhang, Junyi Ge, Hui Zhao, Vivian A. Felde, Chenglong Deng, Maotang Cai, Huan Li, Weihe Ren, Haicheng Wei, Hanfei Yang, Jiawu Zhang, Zicheng Yu, Zhengtang Guo

*Corresponding author. Email: zhaoyan@igsnrr.ac.cn

Published 6 May 2020, *Sci. Adv.* **6**, eaay6193 (2020)
DOI: 10.1126/sciadv.aay6193

The PDF file includes:

Other Supplementary Material for this manuscript includes the following:

(available at advances.sciencemag.org/cgi/content/full/6/19/eaay6193/DC1)

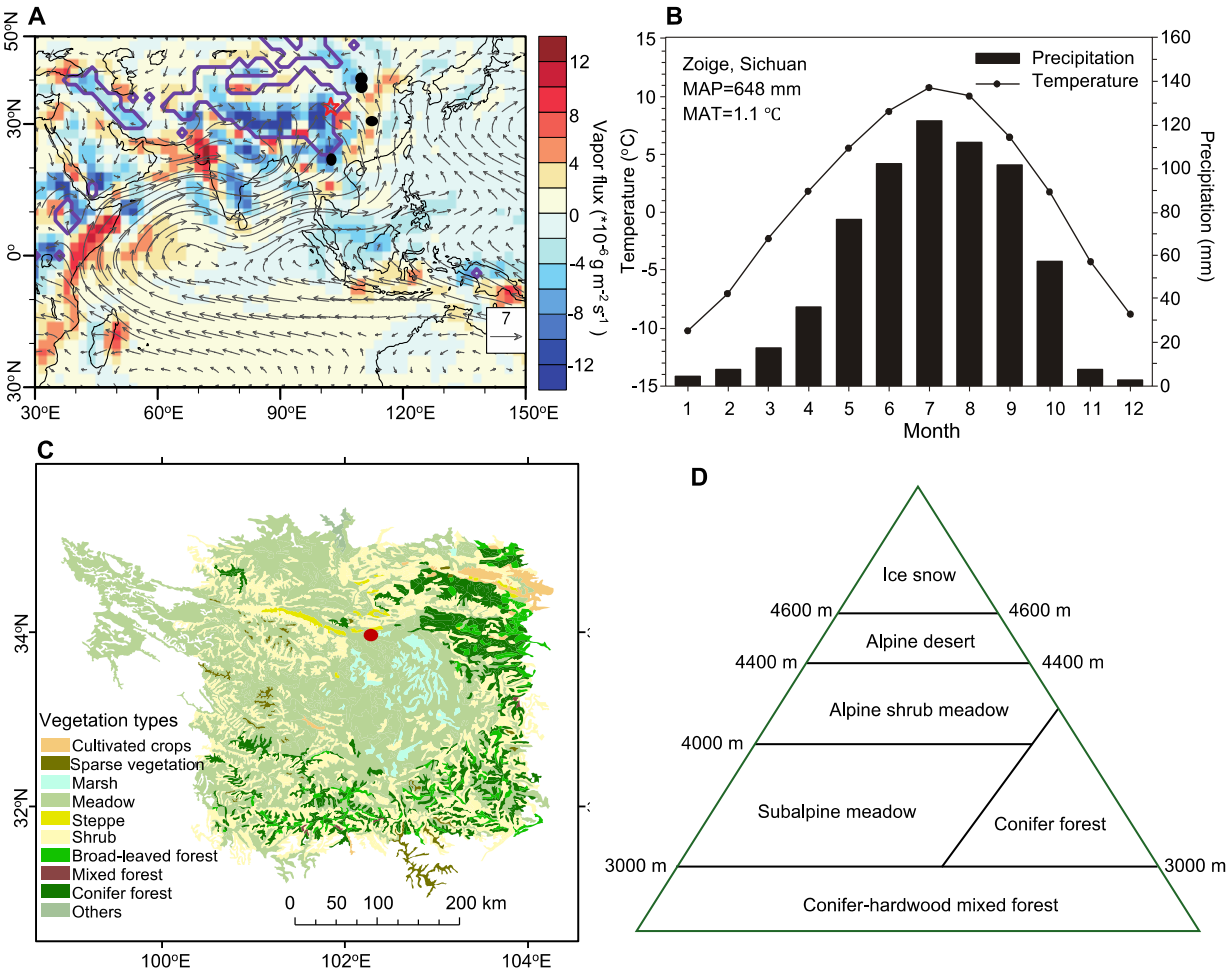

fig. S1. Modern climate and vegetation of the Zoige region, the Tibetan Plateau. (**A**) Location map of the Zoige Basin with the mean 850 hPa streamlines for summer. It is based on the NCEPDOEReanalysis2 data during 1979–2008 provided by the NOAA/OAR/ESRL PSD, Boulder, Colorado, USA, from their website at https://www.esrl.noaa.gov/psd/. The results indicate that the majority of moisture for summer precipitation at Zoige Basin (indicated by red star) comes from the Indian Ocean. The thick purple lines signify the region at the elevation of higher than 1500 m; The units of the vectors are g m^{-1} s^{-1}. The black dots are four previous palaeoclimatic study sites from south to north China: Heqing (*8*), Sanbao Cave (*5*), Lingtai (*13*) and Xifeng Loess (*14*) profiles. (**B**) Climate diagram from the nearby Zoige meteorological station (33°35′ N, 102°58′, 3439 m a.s.l) of our study site in the Zoige Basin. The data are from climate normals for the period 1971-2000. MAP: mean annual precipitation; MAT: mean annual temperature. (**C**) Modern vegetation in the Zoige Basin (indicated by red dot) and the surrounding mountains based on data from website at http://www.geodata.cn/. (**D**) Elevational distribution of vegetation zones in the study region according to the data in Shen et al. (*7*), suggesting that temperature controls tree growth (*6*, *7*).

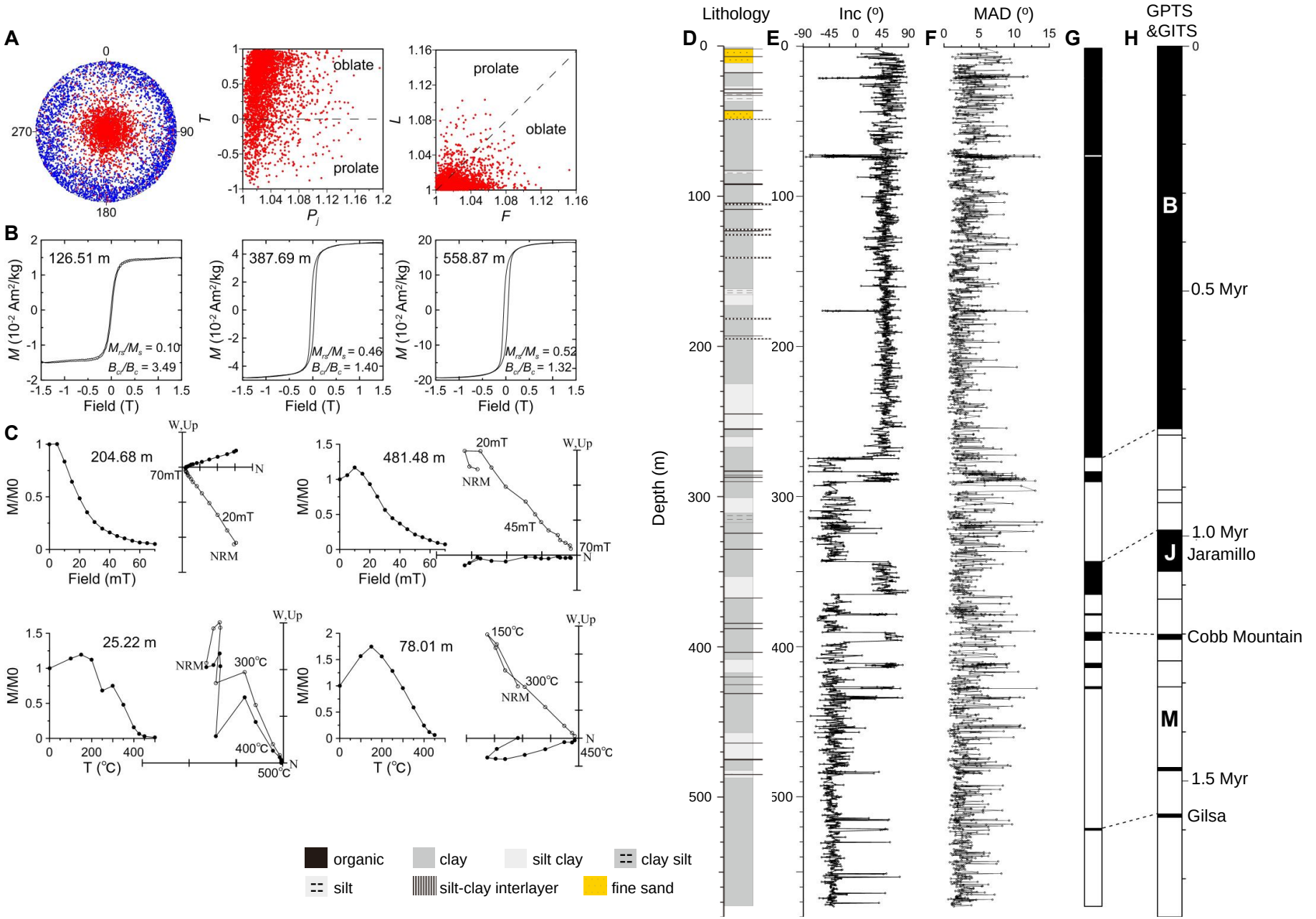

fig. S2. Lithostratigraphy and magnetostratigraphy of the core ZB13-C2 from Zoige Palaeolake. (**A**) Anisotropy of magnetic susceptibility (AMS) characteristics of representative samples. Left panel: Projection of axes of the maximum susceptibility axes (Kmax) (open squares) and the minimum susceptibility axes Kmin (solid circles).

Kmin of the AMS ellipsoid are close to the vertical, perpendicular to the bedding plane, whereas most Kmax are close to the horizontal, parallel to the bedding plane. Middle panel: Corrected degree of susceptibility anisotropy (Pj) versus shape of the anisotropy ellipsoid (T). Right panel: Magnetic lineation (L) versus magnetic foliation (F). Most of F was found to be larger than L, which indicates that the AMS ellipsoid is oblate. The AMS results are typical for an original sedimentary magnetic fabric, indicating that the Zoige Basin sedimentary sequence has not been disturbed since deposition and is suitable for magnetostratigraphic study. (**B**) Hysteresis loops of representative samples after slope correction for paramagnetic contributions. Mrs, Ms, Bc, and Bcr indicate saturation remanent magnetization, saturation magnetization, coercivity, and remanent coercivity, respectively. (**C**) Orthogonal projections of representative progressive alternating field and thermal demagnetization. The solid (open) symbols refer to the horizontal (vertical) plane. As seen in these plots, the secondary viscous remanent magnetization can be mostly removed up to 20 mT (300 ºC), above which a well-defined stable characteristic remanent magnetization is obtained. (**D**) Lithology**.** The sediments mainly consist of clay, silt–clay, and clay–silt, except for two intervals of sand layers at 50.4-40.29 m and 11.28-1.88 m. (**E**) Inclination (Inc.)**.** Clear geomagnetic reversals are identified at 272.26 m, 364.52–343.28 m, and 398.01–390.43 m. (**F**) Maximum angular deviation (MAD): all smaller than 15°, with 98% of the samples having values <10°. (**G**) Magnetic polarity zonation. (**H**) Correlation with the geomagnetic polarity timescale (*61*), indicating the clear Brunhes/Matuyama boundary (272.26 m), and the Jaramillo (364.52–343.28 m) and Cobb-Mountain (398.01–390.43 m) subchrons within the Matuyama chron.

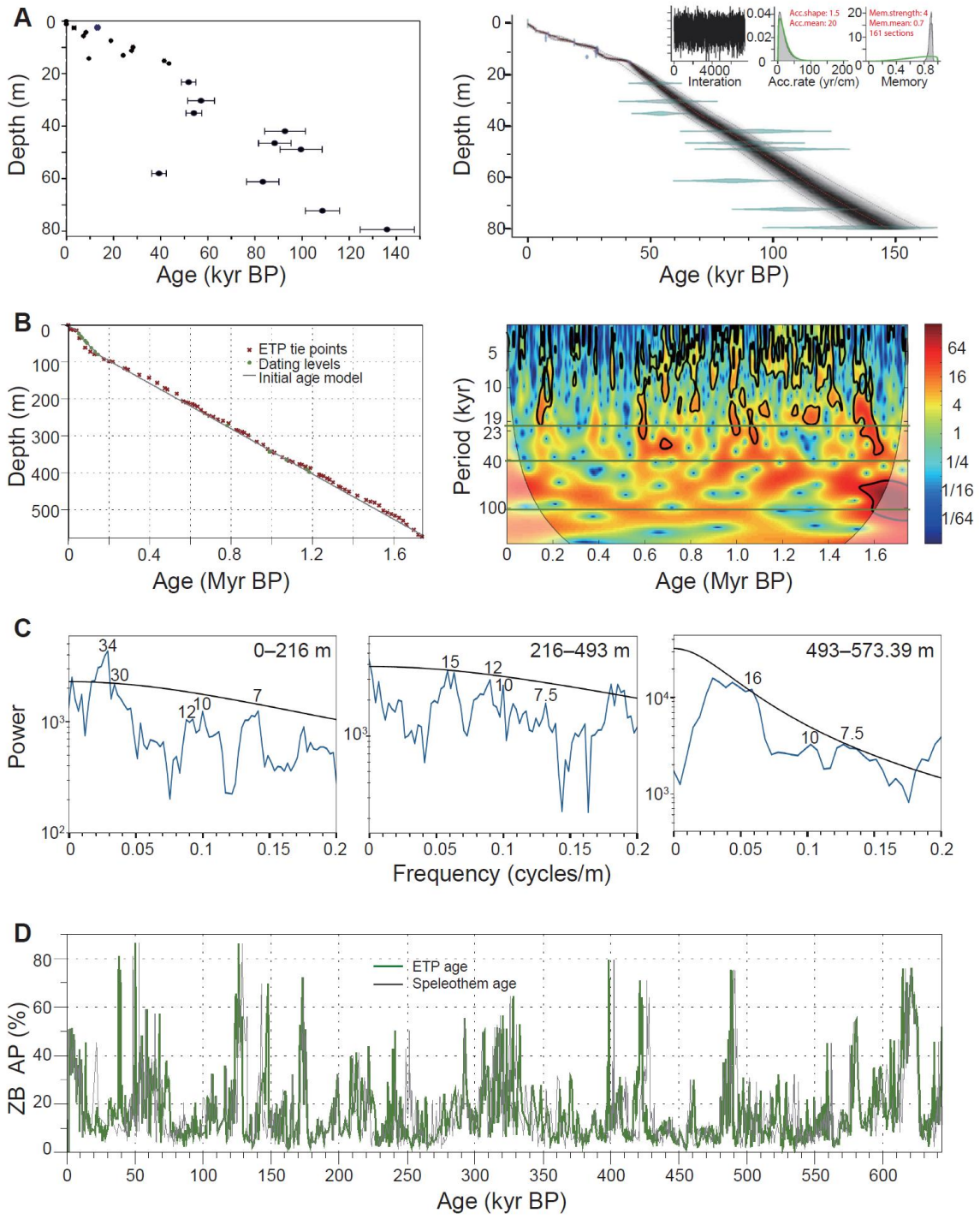

fig. S3. Sensitivity tests of the robustness of the chronology of Zoige Basin core ZB13-C2. (**A**) AMS^{14}C and OSL dates (left panel) and Bayesian age model (right panel) for the top 80 m. (**B**) Correlation of initial age model and ETP tuning age. The initial age model was established using the Bayesian model (above 80 m) and linear regression (below 80 m) based on AMS ^{14}C, OSL and magnetostratigraphy controls. The initial age model yields similar sediment accumulation rates to ETP chronology (left panel). Continuous wavelet transform of AP% based on initial age model (right panel) shows clear orbital periodicities, whose strengths vary in the three intervals as shown by ETP tuning chronology. (**C**) Spectral results of AP% on depth scale. Dominant cyclicity (above 90% confidence level) evolves from 7.5 m/cycle below 493 m, to 15 m/cycle between 216-493 m and 34 m/cycle above 216 m. (**D**) Comparison of AP% based on ETP tuning age model and on age model based on aligning to the Chinese speleothem δ^{18}O (*5*).

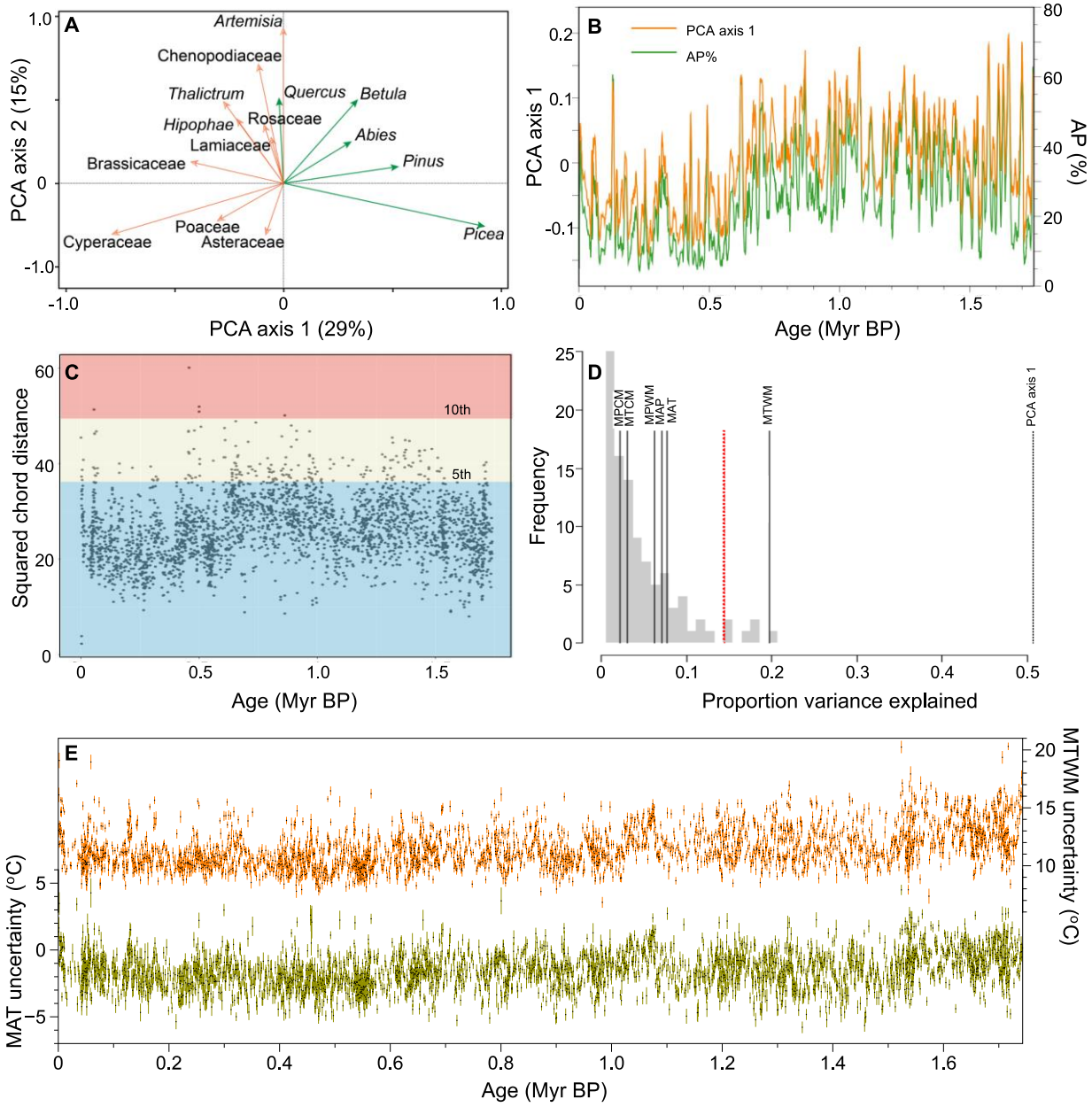

fig. S4. Significance test and uncertainty estimation of pollen-based climate reconstructions for Zoige Basin core ZB13-C2. (**A**) PCA loadings of pollen types, calculated by CANOCO program (*64*). The ordination results indicate that the taxa found with extreme positive values on PCA axis 1, e.g., *Picea*, *Pinus*, and *Betula*, are representative tree taxa of moderate elevation vegetation that occurs under warm and wet conditions, while meadow/steppe taxa found with extreme negative PCA values, e.g., Cyperaceae, are today present under cool and wet conditions (*7*). (**B**) PCA sample scores on axis 1 versus AP%. The weighting of taxa along PCA axis 1, which generally agrees with tree variability, can be interpreted as indicative of a gradient in temperature. **(C)** Analogue quality for the reconstruction of mean temperature of the warmest month (MTWM) based on goodness-of-fit analysis, indicating a good match between fossil samples and modern pollen samples. Blue and red solid lines indicate the 5th and 10th percentiles of the pair-wise distribution of squared-chord distances (*62*) for the calibration sets, respectively. The distances smaller than the 5th percentile of all distances between the calibration-set samples are good "analogues", while distances larger than the 10th percentile are "no-analogue" assemblages. (**D**) Significance test of the reconstructions of mean annual temperature (MAT), MTWM, mean temperature of the coldest month (MTCM), mean annual precipitation (MAP), mean precipitation of the warmest month (MPWM), and

mean precipitation of the coldest month (MPCM). The red line represents the test line of 95% significance level (*63*). The histogram in grey indicates the variance explanatory quantity. MTWM of ZB13-C2 explains more of the variance than 95% of random reconstructions, suggesting it is statistically significant. MAT is the variable that is the closest in the left to the 95% test line. All the precipitation variables fail to pass the significance test, suggesting that the Zoige Basin pollen assemblages are unreliable for precipitation reconstructions. **(E)** Bootstrap sample specific estimates of uncertainties for each reconstructed temperature value.

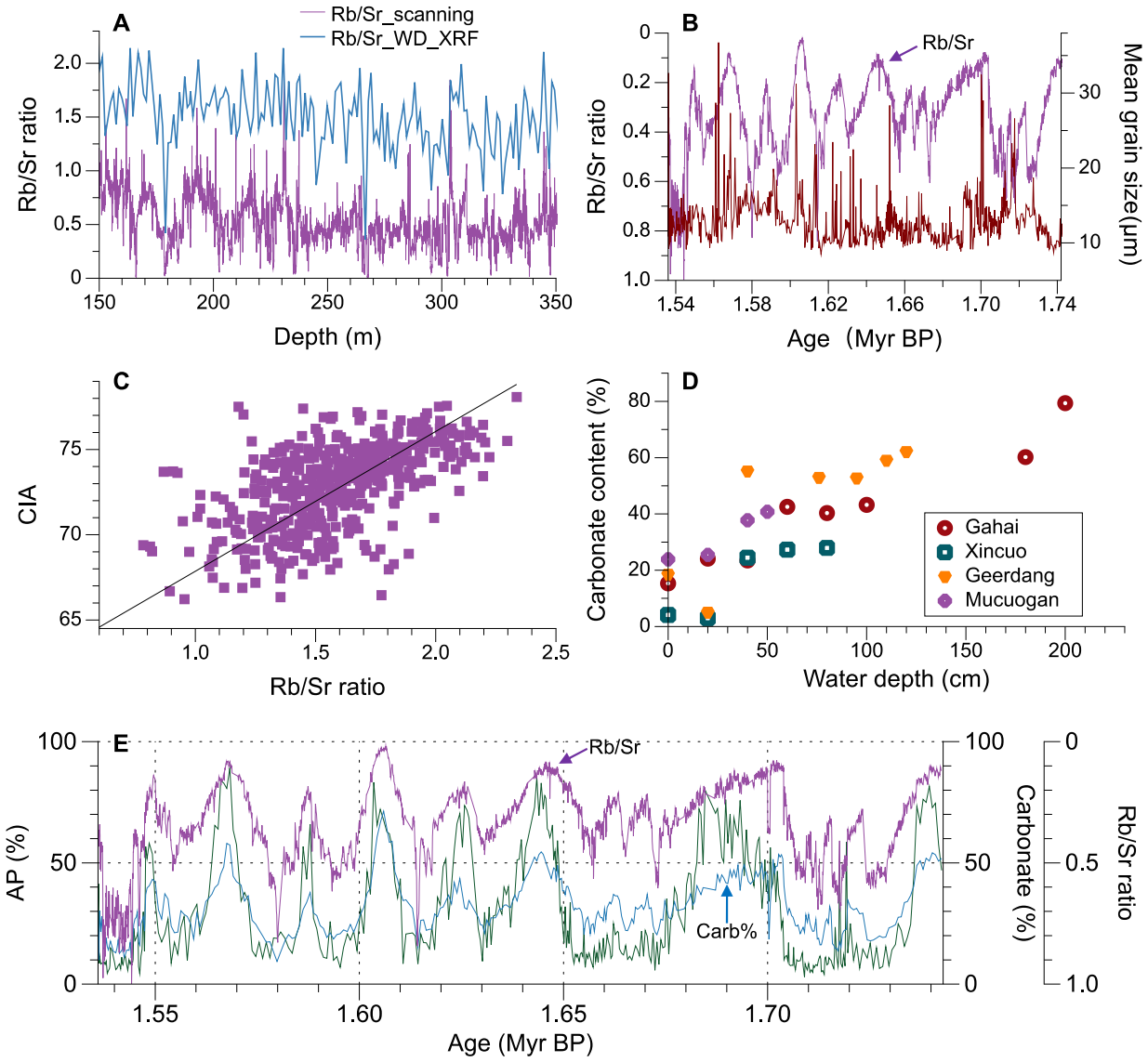

fig. S5. Indication of rubidium/strontium (Rb/Sr) ratio and carbonate content. (**A**) Comparison of the Rb/Sr ratios of Zoige Basin core ZB13-C2 based on XRF scanning and WD-XRF measurements, showing the high coherence. (**B**) Correlation of Rb/Sr ratio (XRF scanning) and mean grain size from ZB13-C2, implying grain size has no major impacts on Rb/Sr ratios. (**C**) Scatter plot of Rb/Sr ratio (WD-XRF measurement) and the chemical index of alteration (CIA) index of the core ZB13-C2. The good correlation between them suggests Rb/Sr is an indicator of weathering. (**D**) Carbonate% along water-depth transects from four lakes in the Zoige region of the eastern Tibetan Plateau. The results generally show increasing carbonate with water depth. The locations of the four lakes are: Gahai Lake (34°14.593′,102°20.416′); Xingcuo Lake (33°51.972′, 102°22.724′); Geerdang Lake (33°19.961′,102°34.060′), and Mucuogan Lake (33°58.694′, 102°32.827′). (**E**) Comparisons of Rb/Sr ratio (XRF sanning) and carbonate% with AP% of core ZB13-C2, indicating their good correlations.

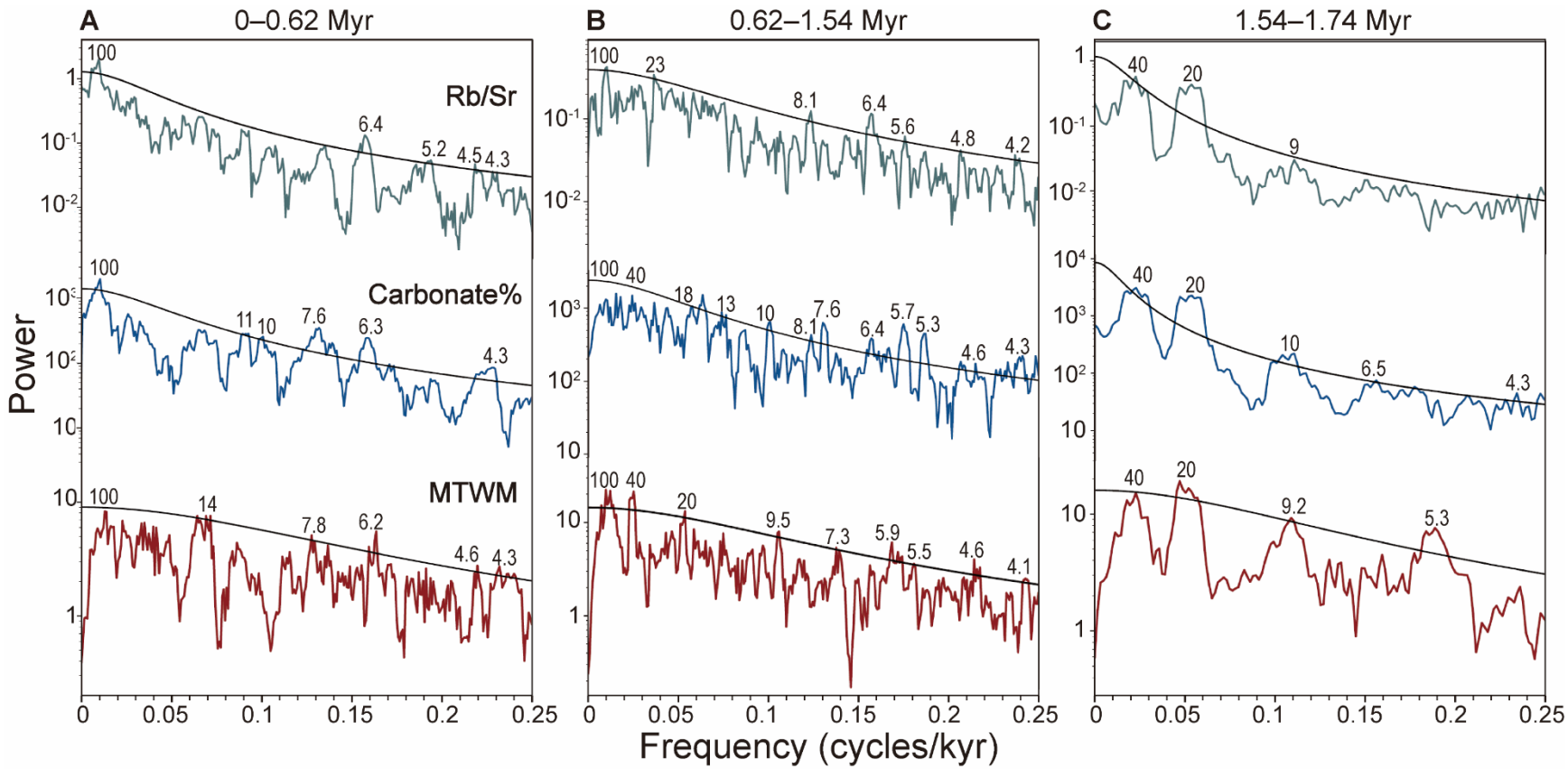

fig. S6. Spectral results of multi-proxies of Zoige Basin core ZB13-C2. (**A**), (**B**) and (**C**) The interval of 0–0.62 Myr BP, 0.62–1.54 Myr BP and 1.54–1.74 Myr BP. The upper, middle and bottom panel is rubidium/strontium (Rb/Sr) ratio, carbonate% and mean temperature of the warmest month (MTWM), respectively. All the data were resampled at equally spaced 0.6-kyr intervals and detrended. Peaks above the 90% confidence levels (black lines) are labelled. They indicate dominant peaks around 100-, 41-, 23-, 11–8-, and 6–4-kyr.

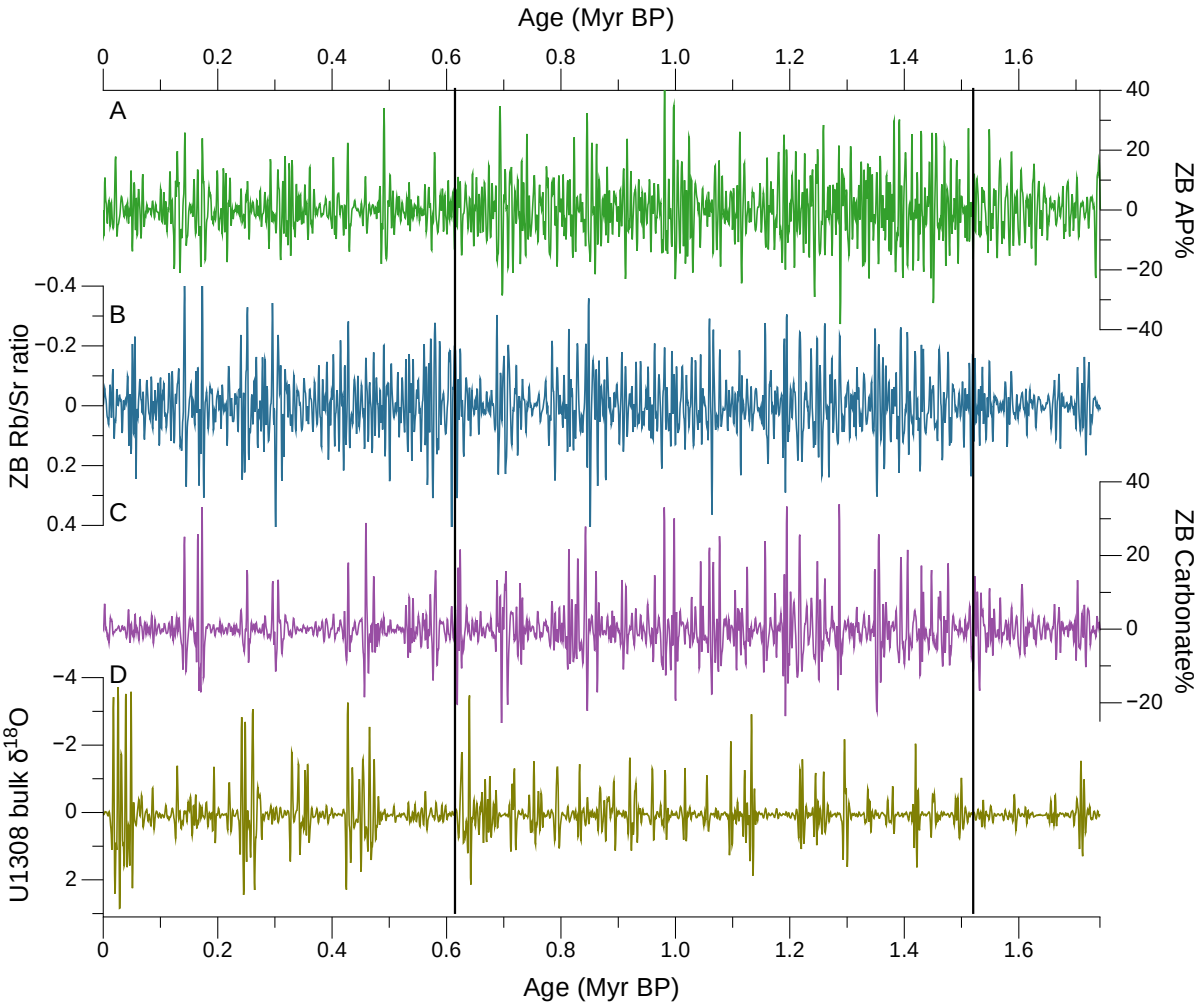

fig. S7. Correlations of millennial variabilities in multi-proxies from Zoige Basin core ZB13-C2 and north Atlantic record. (**A**), (**B**), **and** (**C**) The filtered AP%, Rb/Sr ratio and carbonate% at 15-3 kyr band. (**D**) The filtered $\delta^{18}O$ of bulk carbonate from U1308 (*12*) at 15-3 kyr band, north Atlantic. All the proxies from ZB13-C2 show clear temporal evolution of millennial variabilities at three intervals, which corresponds north Atlantic record.

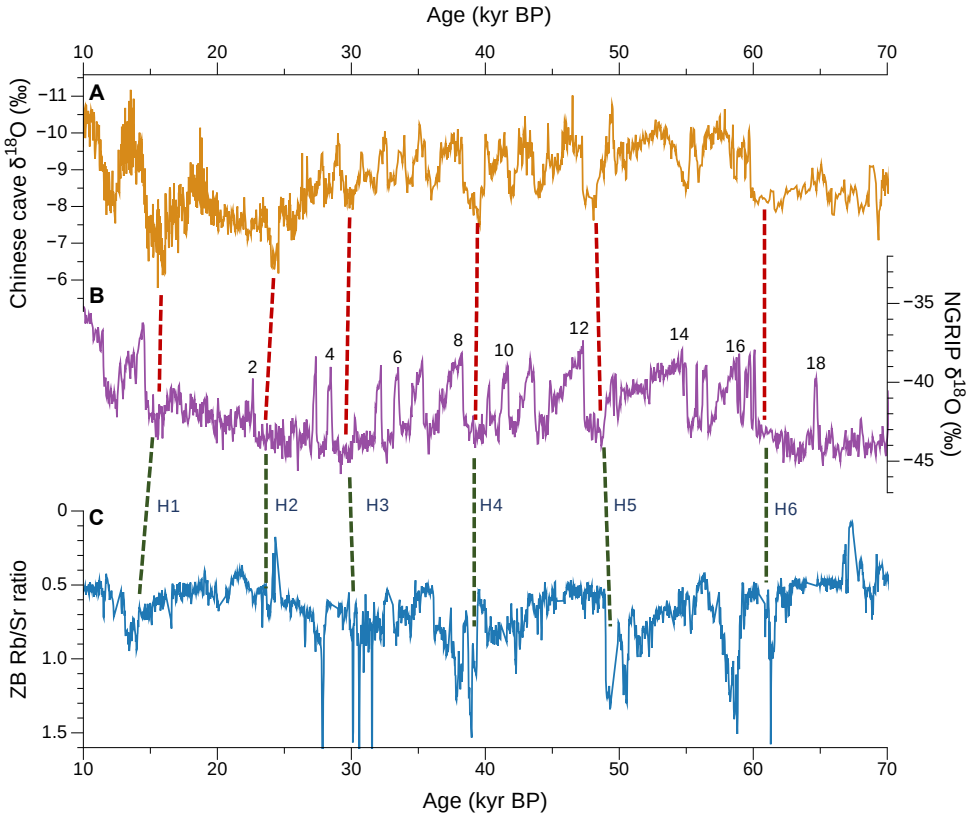

fig. S8. Correlations of millennial variabilities in Rb/Sr ratios from Zoige Basin core ZB13-C2 with NGRIP ice-core and Chinese speleothem records. (**A**) Chinese speleothem $\delta^{18}O$ (*5*). (**B**) $\delta^{18}O$ from the NGRIP ice core, Greenland (*19*). (**C**) Rb/Sr ratio of core ZB 13-C2. Heinrich events (H1 to H6) are well recorded in the Rb/Sr patterns considering the age uncertainty, with high Rb/Sr (low weathering) corresponding to cold events.

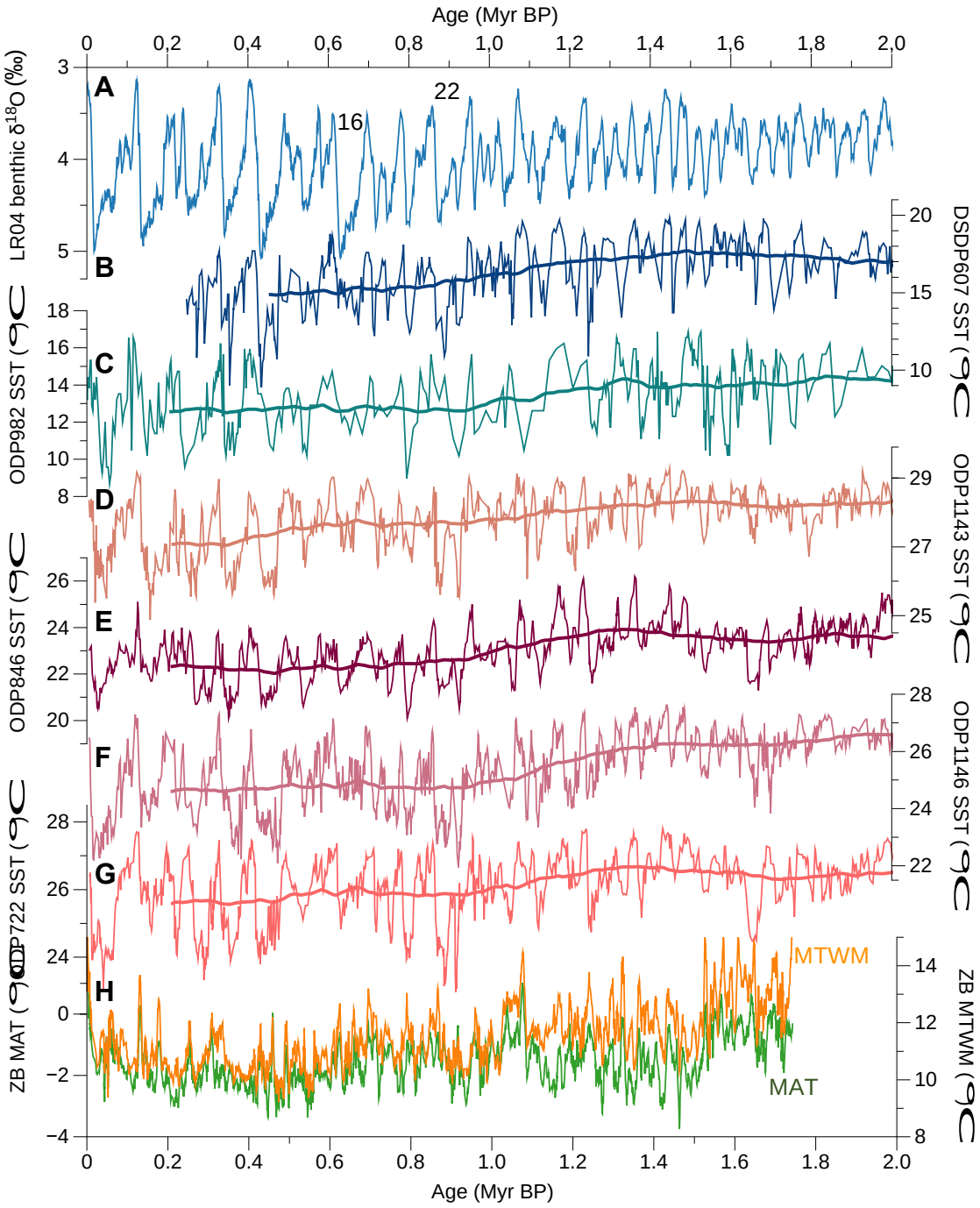

fig. S9. Comparisons of pollen-based temperature reconstructions from Zoige Basin core ZB13-C2 and sea surface temperature (SST). (**A**) LR04 global benthic δ^{18}O stack. The numbers denote the marine isotope stages. (**B**) and (**C**) SST estimates at DSDP site 607 (*20*) and ODP982 (*65*), north Atlantic. (**D**), (**E**) and (**F**) SST at sites of ODP1143 (*66*), ODP846 (*21*) and ODP1146 (*21*) from equatorial Pacific. (**G**) SST at site ODP722 from Arabian Sea (*21*). The thick lines in each SST time series plot are smoothed running means using a 400-kyr window. (**H**) Reconstructed mean temperature of the warmest month (MTWM) and mean annual temperature **(**MAT) (9-point running mean) from ZB13-C2. The general cooling trend are observed for both SST and ZB temperature after ~1.6-1.5 Myr BP.

table S1. AMS radiocarbon dates from Zoige Basin core ZB13-C2.

Lab number	Depth (m)	Material dated	$\delta^{13}C$ (‰ - VPDB)	^{14}C date (yr BP)	Error (±yr)	Calibrated age* (cal yr BP – 2σ range)
Beta-403172	1.17	Sedge leaves+fruits+ 1 piece of wood	-27.1	112.4±0.3 pMC		modern
Beta-455983	2.57	Bulk sample	-24.1	2980	30	3230-3065
Beta-413348	4.27	Sedge leaves +charcoal	-25.3	7410	30	8325-8195
Beta-448696	5.63	Sedge leaves	-26.5	6320	30	7310-7175
Beta-395809	7.45	Sedge leaves+*Phragmites* leave	-24.4	15610	50	18935-18770
Beta-400979	9.93	Sedge leaves	-26	24170	100	28445-27955
Beta-413349	11.27	Sedge leaves+*Phragmites* leaves	-25.6	23520	80	27760-27580
Beta-403171	13.03	Sedge leaves	-26.6	19970	80	24195-23865
Beta-455984	14.23	Bulk sample	-24.4	8520	30	9540-9485
Beta-455985	15.15	Bulk sample	-24.3	36890	310	41930-40965
Beta-394871	16.14	Sedge leaves	-25.3	>43500		>43500

*Calibration was calculated using the database associated with the 2013 INTAL program (*67*)

table S2. OSL dates from Zoige Basin core ZB13-C2.

Lab#	Depth (m)	Number of Aliquots	Equivalent Dose (Gy)	U (ppm)	Th (ppm)	K (%)	Water content (%)	Cosmic Ray dose rate (Gy/ka)	Total dose rate (Gy/ka)	Age (kyr)
IOSL2014-20	2.45	10	33.65±0.65	1.39±0.08	8.40±0.25	1.48±0.05	10.7	0.3	2.55±0.15	13.17±0.43
IOSL2014-21	23.29	8	141.22±1.96	1.63±0.08	8.45±0.25	1.53±0.05	18.1	0.04	2.72±0.15	51.84±3.05
IOSL2015-10	30.34	10	154.18±4.63	2.46±0.10	10.6±0.29	1.72±0.06	26.1	0.05	2.71±0.19	57.12±5.68
IOSL2014-22	35.05	10	152.45±3.22	2.19±0.09	11.2±0.30	1.81±0.04	23.1	0.02	2.81±0.16	54.07±3.35
IOSL2015-11	41.96	8	209.64±5.44	1.76±0.08	7.73±0.23	1.31±0.05	21.7	0.04	2.26±0.16	92.77±8.71
IOSL2014-23	46.53	10	267.83±14.27	2.14±0.09	10.0±0.28	1.87±0.06	17.6	0.01	3.02±0.17	88.40±6.89
IOSL2015-12	48.92	10	249.78±10.62	1.87±0.09	8.06±0.24	1.61±0.05	21.4	0.02	2.52±0.18	99.54±8.94
IOSL2014-24	58.06	10	126.83±9.69	2.16±0.09	13.4±0.29	2.62±0.05	21.3	0.01	3.21±0.20	39.25±3.12
IOSL2015-13	61.22	10	299.75±12.26	2.62±0.10	15.2±0.31	2.70±0.07	27.8	0.01	3.60±0.26	83.34±6.85
IOSL2014-25	72.29	10	401.11±18.43	2.64±0.10	14.0±0.37	2.44±0.06	18.2	0.01	3.69±0.20	108.67±7.23
IOSL2015-14	79.43	10	443.27±22.51	2.38±0.09	13.1±0.30	2.05±0.06	21.3	0.01	3.26±0.22	136.08±11.5

Notes: All samples were measured on K-Fs (*68*) using MET IRSL method. The grain size used for measurement is 90-125 μm.

table S3. Age control points and AP% data of Zoige Basin core ZB 13-C2.
(Please see separate excel file)

table S4. Error estimates of climate variables for locally-weighted weighted-average partial least squares (LWWAPLS) model using various numbers of analogues. The variables include mean annual temperture (MAT), mean temperature of the warmest month (MTWM) and mean annual precipitation (MAP). Model errors are given as root mean square errors of prediction (RMSEP) calculated by leave-one-out cross-validation.

Variables	RMSEP_20 analogues	RMSEP_25 analogues	RMSEP_30 analogues	RMSEP_50 analogues
MAT	3.0559	3.1416	3.1498	3.2044
MTWM	3.4282	4.3481	4.0843	4.4109
MAP	169.6246	157.2452	157.0040	160.3852

table S5. Performance statistics of the LWWAPLS climate reconstruction method applied in this study. It gives the coefficient of determination (R^2), the average and maximum bias of the reconstruction, and the root mean square error of prediction (RMSEP) for mean annual temperature (MAT), mean temperature of the warmest month (MTWM), annual precipitation (MAP), and mean precipitation of the coldest month (MPCM).

Climate variable	RMSEP*	R^2	Average bias	Maximum bias
MAT	3.0559	0.8609	0.2097	6.0350
MTWM	3.4282	0.8146	0.0193	9.5080
MAP	169.6246	0.7049	6.3386	181.6490
MPCM	3.5621	0.8566	0.3472	27.3499

Notes: *RMSEP could be misleading for LWWAPLS approach, while the significance test is a better validation method.

REFERENCES AND NOTES

1. M. Abe, M. Hori, T. Yasunari, A. Kitoh, Effects of the Tibetan Plateau on the onset of the summer monsoon in South Asia: The role of the air-sea interaction. *J. Geophys. Res. Atmos.* **118**, 1760–1776 (2013).

2. H. Lü, S. Wang, N. Wu, G. Tong, X. Yang, C. Shen, S. Li, L. Zhu, L. Wang, A new pollen record of the last 2.8 Ma from the Co Ngoin, central Tibetan Plateau. *Sci. China* **44**, 292–300 (2001).

3. F. H. Chen, J. Bloemendal, P. Z. Zhang, G. X. Liu, An 800 ky proxy record of climate from lake sediments of the Zoige Basin, eastern Tibetan Plateau. *Palaeogeogr. Palaeoclimatol. Palaeoecol.* **151**, 307–320 (1999).

4. J. Laskar, P. Robutel, F. Joutel, M. Gastineau, A. C. M. Correia, B. Levrard, A long-term numerical solution for the insolation quantities of the Earth. *Astron. Astrophys.* **428**, 261–285 (2004).

5. H. Cheng, R. L. Edwards, A. Sinha, C. Spötl, L. Yi, S. Chen, M. Kelly, G. Kathayat, X. Wang, X. Li, X. Kong, Y. Wang, Y. Ning, H. Zhang, The Asian monsoon over the past 640,000 years and ice age terminations. *Nature* **534**, 640–646 (2016).

6. X. Y. Hou, *Vegetation Atlas of China (Scale: 1:1,000,000)* (Science Press, Beijing, 2001).

7. C. Shen, L. Tang, S. Wang, C. Li, K.-b. Liu, Pollen records and time scale for the RM core of the Zoige Basin, northeastern Qinghai-Tibetan Plateau. *Chin. Sci. Bull.* **50**, 553–562 (2005).

8. Z. S. An, S. C. Clemens, J. Shen, X. Qiang, Z. Jin, Y. Sun, W. L. Prell, J. Luo, S. Wang, H. Xu, Y. Cai, W. Zhou, X. Liu, W. Liu, Z. Shi, L. Yan, X. Xiao, H. Chang, F. Wu, L. Ai, F. Lu, Glacial-interglacial Indian summer monsoon dynamics. *Science* **333**, 719–723 (2011).

9. A. Donohoe, J. Marshall, D. Ferreira, D. McGee, The relationship between ITCZ location and cross-equatorial atmospheric heat transport: From the seasonal cycle to the last glacial maximum. *J. Climate* **26**, 3597–3618 (2013).

10. L. E. Lisiecki, M. E. Raymo, A Pliocene-Pleistocene stack of 57 globally distributed benthic $\delta^{18}O$ records. *Paleoceanography* **20**, PA1003 (2005).

11. D. A. Hodell, J. E. T. Channell, Mode transitions in Northern Hemisphere glaciation: Co-evolution of millennial and orbital variability in Quaternary climate. *Clim. Past* **12**, 1805–1828 (2016).

12. G. C. H. Chiang, I. Y. Fung, C.-H. Wu, Y. Cai, J. P. Edman, Y. Liu, J. A. Day, T. Bhattacharya, Y. Mondal, C. A. Labrousse, Role of seasonal transitions and westerly jets in East Asian paleoclimate. *Quat. Sci. Rev.* **108**, 111–129 (2015).

13. Z. L. Ding, E. Derbyshire, S. L. Yang, Z. W. Yu, S. F. Xiong, T. S. Liu, Stacked 2.6-Ma grain size record from the Chinese loess based on five sections and correlation with the deep-sea $\delta^{18}O$ record. *Paleoceanography* **17**, 5-1-5-21 (2002).

14. Z. Guo, P. Biscaye, L. Wei, X. hen, S. Peng, T. Liu, Summer monsoon variations over the last 1.2 Ma from the weathering of loess-soil sequences in China. *Geophys. Res. Lett.* **27**, 1751–1754 (2000).

15. Y. Sun, Q. Yin, M. Crucifix, S. C. Clemens, P. Araya-Melo, W. Liu, X. Qiang, Q Liu, H. Zhao, L. Liang, H. Chen, Y. Li, L. Zhang, G. Dong, M. Li, W. Zhou, A. Berger, Z. An, Diverse manifestations of the mid-Pleistocene climate transition. *Nat. Commun.* **10**, 352 (2019).

16. M. E. Raymo, K. Ganley, S. Carter, D. W. Oppo, J. McManus, Millennial-scale climate instability during the early Pleistocene epoch. *Nature* **392**, 699–702 (1998).

17. A. Berger, M. F. Loutre, J. L. Mélice, Equatorial insolation: From precession harmonics to eccentricity frequencies. *Clim. Past* **2**, 131–136 (2006).

18. C. S. M. Turney, A. P. Kershaw, S. C. Clemens, N. Branch, P. T. Moss, L. K. Fifield, Millennial and orbital variations of El Niño/Southern Oscillation and high-latitude climate in the last glacial period. *Nature* **428**, 306–310 (2004).

19. North Greenland Ice Core Project Members. High-resolution record of the Northern Hemisphere climate extending into the last interglacial period. *Nature* **431**, 147–151 (2004).

20. K. T. Lawrence, S. Sosdian, H. E. White, Y. Rosenthal, North Atlantic climate evolution through the Plio-Pleistocene climate transitions. *Earth Planet. Sci. Lett.* **300**, 329–342 (2010).

21. T. D. Herbert, L. C. Peterson, K. T. Lawrence, Z. Liu, Tropical ocean temperatures over the past 3.5 million years. *Science* **328**, 1530–1534 (2010).

22. E. L. McClymont, S. M. Sosdian, A. Rosell-Melé, Y. Rosenthal, Pleistocene sea-surface temperature evolution: Early cooling, delayed glacial intensification, and implications for the mid-Pleistocene climate transition. *Earth Sci. Rev.* **123**, 173–193 (2013).

23. H. Elderfield, P. Ferretti, M. Greaves, S. Crowhurst, I. N. McCave, D. Hodell, A. M. Piotrowski, Evolution of ocean temperature and ice volume through the mid-Pleistocene climate transition. *Science* **337**, 704–709 (2012).

24. M. E. Raymo, The timing of major climate terminations. *Paleoceanography* **12**, 577–585 (1997).

25. P. C. Tzedakis, M. Crucifix, T. Mitsui, W. Wolff, A simple rule to determine which insolation cycles lead to interglacials. *Nature* **542**, 427–432 (2017).

26. P. U. Clark, D. Archer, D. Pollard, J. D. Blum, J. A. Rial, V. Brovkin, A. C. Mix, N. G. Pisias, M. Roy, The middle Pleistocene transition: Characteristics, mechanisms and implications for long-term changes in atmospheric pCO_2. *Quat. Sci. Rev.* **25**, 3150–3184 (2006).

27. T. B. Chalk, M. P. Hain, G. L. Foster, E. J. Rohling, P. F. Sexton, M. P. S. Badger, S. G. Cherry, A. P. Hasenfratz, G. H. Haug, S. L. Jaccard, A. Martínez-García, H. Pälike, R. D. Pancost, P. A. Wilson, Causes of ice age intensification across the Mid-Pleistocene Transition. *Proc. Natl. Acad. Sci. U.S.A.* **114**, 13114–13119 (2017).

28. M. Willeit, A. Ganopolski, R. Calov, V. Brovkin, Mid-Pleistocene transition in glacial cycles explained by declining CO_2 and regolith removal. *Sci. Adv.* **5**, eaav7337 (2019)

29. B. Hönisch, N. G. Hemming, D. Archer, M. Siddall, J. F. McManus, Atmospheric carbon dioxide concentration across the mid-Pleistocene transition. *Science* **324**, 1551–1553 (2009).

30. Y. Yan, M. L. Bender, E. J. Brook, H. M. Clifford, P. C. Kemeny, A.V. Kurbatov, S. Mackay, P. A. Mayewski, J. Ng, J. P. Severinghaus, J. A. Higgins, Two-million-year-old snapshots of atmospheric gases from Antarctic ice. *Nature* **574**, 663–666 (2019).

31. K. A. Dyez, B. Hönisch, G. A. Schmidt, Early Pleistocene obliquity-scale pCO_2 variability at ~1.5 million years ago. *Paleoceanography* **33**, 1270–1291 (2018).

32. J. R. Farmer, B. Hönisch, L. L. Haynes, D. Kroon, S. Jung, H. L. Ford, M. E. Raymo, M. Jaume-Seguí, D. B. Bell, S. L. Goldstein, L. D. Pena, M. Yehudai, J. Kim, Deep Atlantic ocean carbon storage and the rise of 100,000-year glacial cycle. *Nat. Geosci.* **12**, 355–360 (2019).

33. A. Martínez-Garcia, A. Rosell-Melé, S. L. Jaccard, W. Geibert, D. M. Sigman, G. H. Haug, Southern Ocean dust–climate coupling over the past four million years. *Nature* **476**, 312–315. (2011).

34. D. A. Hodell, K. A. Venz-Curtis, Late Neogene history of deepwater ventilation in the Southern ocean. *Geochem. Geophys. Geosyst.* **7**, Q09001 (2006).

35. D. Lüthi, M. Le Floch, B. Bereiter, T. Blunier, J.-M. Barnola, U. Siegenthaler, D. Raynaud, J. Jouzel, H. Fischer, K. Kawamura, T. F. Stocker, High-resolution carbon dioxide concentration record 650,000–800,000 years before present. *Nature* **453**, 379–382 (2008).

36. B. Bereiter, S. Eggleston, J. Schmitt, C. Nehrbass-Ahles, T. F. Stocker, H. Fischer, S. Kipfstuhl, J. Chappellaz, Revision of the EPICA Dome C CO_2 record from 800 to 600 kyr before present. *Geophys. Res. Lett.* **42**, 542–549 (2015).

37. D. A. Hodell, J. E. T. Channell, J. H. Curtis, O. E. Romero, U. Röhl, Onset of "Hudson Strait" Heinrich events in the eastern North Atlantic at the end of the middle Pleistocene transition (~640 ka)? *Paleoceanography* **23**, PA4218 (2008).

38. P. D. Hughes, P. L. Gibbard, Global glacier dynamics during 100 ka Pleistocene glacial cycles. *Quatern. Res.* **90**, 222–243 (2018).

39. Past Interglacials Working Group of PAGES, Interglacials of the last 800,000 years. *Rev. Geophys.* **54**, 162–219 (2016).

40. J. Li, X. Fang, C. Song, B. Pan, Y. Ma, M. Yan, Late Miocene–Quaternary rapid stepwise uplift of the NE Tibetan Plateau and its effects on climatic and environmental changes. *Quatern. Res.* **81**, 400–423 (2014)

41. A. Copley, J.-P. Avouac, B. P. Wernicke, Evidence for mechanical coupling and strong Indian lower crust beneath southern Tibet. *Nature* **472**, 79–81 (2011).

42. P. Molnar, J. M. Stock, Slowing of India's convergence with Eurasia since 20 Ma and its implications for Tibetan mantle dynamics. *Tectonics* **28**, TC3001 (2009).

43. J. Quade, D. O. Breecker, M. Daëron, J. Eiler, The paleoaltimetry of Tibet: An isotopic perspective. *Am. J. Sci.* **311**, 77–115 (2011).

44. B. S. Currie, P. J. Polissar, D. B. Rowley, M. Ingalls, S. Li, G. Olake, K. H. Freeman, Multiproxy paleoaltimetry of the Late Oligocene-Pliocene Oiyug Basin, Southern Tibet. *Am. J. Sci.* **316**, 401–436 (2016).

45. C. Thiel, J.-P. Buylaert, A. Murray, B. Terhorst, I. Hofer, S. Tsukamoto, M. Frechen, Luminescence dating of the Stratzing loess profile (Austria) – Testing the potential of an elevated temperature post-IR IRSL protocol. *Quat. Int.* **234**, 23–31 (2011).

46. B. Li, S.-H. Li, Luminescence dating of K-feldspar from sediments: A protocol without anomalous fading correction. *Quat. Geochronol.* **6**, 468–479 (2011).

47. A. G. Wintle, Anomalous fading of thermo-luminescence in mineral samples. *Nature* **245**, 143–144 (1973).

48. G. Adamiec, M. J. Aitken, Dose-rate conversion factors: Update. *Ancient TL* **16**, 37–50 (1998).

49. H. Zhao, S.-H. Li, Internal dose rate to K-feldspar grains from radioactive elements other than potassium. *Radiat. Meas.* **40**, 84–93 (2005).

50. V. Jelínek, V. Kropáček, Statistical processing of anisotropy of magnetic susceptibility measured on groups of specimens. *Stud. Geophys. Geod.* **22**, 50–62 (1978).

51. P. Vlag, N. Thouveny, D. Williamson, P. Rochette, F. Ben-Atig, Evidence for a geomagnetic excursion recorded in the sediments of Lac St. Front, France: A link with the Laschamp excursion? *J. Geophys. Res.* **101**, 28211–28230 (1996).

52. C. Deng, R. Zhu, M. J. Jackson, K. L. Verosub, M. J. Singer, Variability of the temperature-dependent susceptibility of the Holocene eolian deposits in the Chinese loess plateau: A pedogenesis indicator. *Phys. Chem. Earth* **26**, 873–878 (2001).

53. W. E. Dean, Determination of carbonate and organic matter in calcareous sediments and sedimentary rocks by loss on ignition; comparison with other methods. *J. Sediment. Res.* **44**, 242–248 (1974).

54. K. Faegri, J. Iversen, *Textbook of Pollen Analysis* (Wiley, 1989).

55. E. C. Grimm, CONISS: A FORTRAN 77 program for stratigraphically constrained cluster analysis by the method of incremental sum of squares. *Comput. Geosci.* **13**, 13–35 (1987).

56. J. Ni, G. Yu, S. P. Harrison, I. C. Prentice, Palaeovegetation in China during the late Quaternary: Biome reconstructions based on a global scheme of plant functional types. *Palaeogeogr. Palaeoclimatol. Palaeoecol.* **289**, 44–61 (2010).

57. J. Guiot, C. Goeury, PPPBase, a software for statistical analysis of paleoecological and paleoclimatological data. *Dendrochronologia* **14**, 295–300 (1996).

58. H. J. B. Birks, A. F. Lotter, S. Juggins, J. P. Smol, *Tracking Environmental Change Using Lake Sediments: Data Handling and Numerical Techniques* (Dordrecht, Springer Netherlands, 2012), vol. 5.

59. R. Vautard, P. Yiou, M. Ghil, Singular-spectrum analysis: A toolkit for short, noisy chaitic signals. *Physics D* **58**, 95–126 (1992).

60. A. Grinsted, J. C. Moore, S. Jevrejeva, Application of the cross wavelet transform and wavelet coherence to geophysical time series. *Nonlin. Processes Geophys.* **11**, 561–566 (2004).

61. F. J. Hilgen, L. J. Lourens, J. A. van Dam, The Neogene period in *The Geologic Time Scale*, F. M. Gradstein, J. G. Ogg, M. D. Schmitz, G. M. Ogg, Eds. (Elsevier, Boston, 2012).

62. J. T. Overpeck, T. Webb III, I. C. Prentice, Quantitative interpretation of fossil pollen spectra: Dissimilarity coefficients and the method of modern analogs. *Quatern. Res.* **23**, 87–108 (1985).

63. R. J. Telford, H. J. B. Birks, A novel method for assessing the statistical significance of quantitative reconstructions inferred from biotic assemblages. *Quat. Sci. Rev.* **30**,1272–1278 (2011).

64. C. J. F. ter Braak, CANOCO-a FORTRAN program for canonical community ordination by [partial] [detrended] [canonical] correspondence analysis, principal components analysis and redundancy analysis version 2.1 (Agricultural Mathematics Group, Wageningen, The Netherlands, 1988).

65. T. D. Herbert, K. T. Lawrence, A. Tzanova, L. C. Peterson, R. Caballero-Gill, C. S. Kelly, Late Miocene global cooling and the rise of modern ecosystems. *Nat. Geosci.* **9**, 843–847 (2016).

66. L. Li, Q. Li, J. Tian, P. Wang, H. Wang, Z. Liu, A 4-Ma record of thermal evolution in the tropical western Pacific and its implications on climate change. *Earth Planet. Sci. Lett.* **309**, 10–20 (2011).

67. P. J. Reimer, E. Bard, A. Bayliss, J. W. Beck, P. G. Blackwell, C. B. Ramsey, C. E. Buck, H. Cheng, R. L. Edwards, M. Friedrich, P. M. Grootes, T. P. Guilderson, H. Haflidason, I. Hajdas, C. Hatté, T. J. Heaton, D. L. Hoffmann, A. G. Hogg, K. A. Hughen, K. F. Kaiser, B. Kromer, S. W. Manning, M. Niu, R. W. Reimer, D. A. Richards, E. M. Scott, J. R. Southon, R. A. Staff, C. S. M. Turney, J. van der Plicht, Intcal13 and Marine13 radiocarbon age calibration curves 0–50,000 years cal BP. *Radiocarbon* **55**, 1869–1887 (2013).

68. D. J. Huntley, M. Baril, The K content of the K-feldspars being measured in optical dating or in thermoluminescence dating. *Ancient TL* **15**, 11–13 (1997).